AGU PUBLICATIONS

JGR

Journal of Geophysical Research: Oceans

RESEARCH ARTICLE

10.1002/2014JC010211

Key Points:
- Deep fronts induce mesoscale-submesoscale coupling
- Existing parameterizations are approximately able to reproduce such coupling
- Deep fronts enhance tracer transport into the mixed layer

Correspondence to:
S. Ramachandran,
sramachandran@umassd.edu

Citation:
Ramachandran, S., A. Tandon, and A. Mahadevan (2014), Enhancement in vertical fluxes at a front by mesoscale-submesoscale coupling, *J. Geophys. Res. Oceans*, *119*, 8495–8511, doi:10.1002/2014JC010211.

Received 15 JUN 2014
Accepted 19 NOV 2014
Accepted article online 24 NOV 2014
Published online 12 DEC 2014

Enhancement in vertical fluxes at a front by mesoscale-submesoscale coupling

Sanjiv Ramachandran[1], Amit Tandon[1,2], and Amala Mahadevan[3]

[1]Department of Mechanical Engineering, University of Massachusetts, Dartmouth, Massachusetts, USA, [2]School of Marine Sciences, University of Massachusetts, Dartmouth, Massachusetts, USA, [3]Woods Hole Oceanographic Institution, Woods Hole, Massachusetts, USA

Abstract Oceanic frontal instabilities are of importance for the vertical exchange of properties in the ocean. Submesoscale, O(1) Rossby number, dynamics are particularly relevant for inducing the vertical (and lateral) flux of buoyancy and tracers in the mixed layer, but how these couple with the stratified pycnocline is less clear. Observations show surface fronts often persist beneath the mixed layer. Here we use idealized, three-dimensional model simulations to show how surface fronts that extend deeper into the pycnocline invoke enhanced vertical fluxes through the coupling of submesoscale and mesoscale instabilities. We contrast simulations in which the front is restricted to the mixed layer with those in which it extends deeper. For the deeper fronts, we examine the effect of density stratification on the vertical coupling. Our results show deep fronts can dynamically couple the mixed layer and pycnocline on time scales that increase with the peak stratification beneath the mixed layer. Eddies in the interior generate skew fluxes of buoyancy and tracer oriented along isopycnals, thus providing an adiabatic pathway for the interior to interact with the mixed layer at fronts. The vertical enhancement of tracer fluxes through the mesoscale-submesoscale coupling described here is thus relevant to the vertical supply of nutrients for phytoplankton in the ocean. A further implication for wind-forced fronts is that the vertical structure of the stream function characterizing the exchange between the interior and the mixed layer exhibits significant qualitative differences compared to a linear combination of existing parameterizations of submesoscale eddies in the mixed layer and mesoscale eddies in the interior. The discrepancies are most severe within the mixed layer suggesting a potential role for Ekman-layer dynamics absent in existing submesoscale parameterizations.

1. Introduction

Mixed-layer density fronts are an important source of unbalanced motions in the upper ocean. The departure from balance arises from three-dimensional, ageostrophic instabilities in the mixed layer (MLI) [*Boccaletti et al.*, 2007; *Fox-Kemper et al.*, 2008; *Akitomo*, 2010] that convert the available potential energy (APE) residing in the front to eddy kinetic energy. Loss of balance can also occur via two-dimensional instabilities such as symmetric instability (SI) induced by the destruction of potential vorticity at fronts forced by down-front winds (aligned with the geostrophic current) [*Thomas*, 2005] or surface cooling [*Taylor and Ferrari*, 2010; *Thomas and Taylor*, 2010]. Nonlinear simulations show MLI eventually replaces SI as the sole mechanism for the extraction of APE [*Fox-Kemper et al.*, 2008] once the Richardson number increases beyond unity, thus precluding the onset of SI. The eddies resulting from MLI are O(1–10 km), or submesoscale, evolve over inertial time scales, and are characterized by O(1) Rossby number (*Ro*) [*Mahadevan*, 2006; *D'Asaro et al.*, 2011; *Özgökmen et al.*, 2012; *Capet et al.*, 2008a; *Klein et al.*, 2008; *Fox-Kemper et al.*, 2008].

The intense vertical motions generated by submesoscale instabilities can give rise to large vertical tracer fluxes, which has important implications for the transport of nutrients and biological activity in the upper ocean [*Mahadevan and Archer*, 2000; *Lévy et al.*, 2001]. Submesoscale-resolving simulations show large vertical velocities O(50–100 m)/d along narrow filaments O(5–10 km) wide at the edges of fronts [*Capet et al.*, 2008b; *Klein and Lapeyre*, 2009; *Mahadevan and Tandon*, 2006; *Mahadevan*, 2006]. The upwelling velocities at the frontal edges can be 1–2 orders of magnitude larger than those achieved by linear Ekman pumping [*Mahadevan et al.*, 2008].

Simulations show that the restratification by MLI is of leading order in the mixed-layer buoyancy budget [*Fox-Kemper et al.*, 2008; *Capet et al.*, 2008a]. The increase in stratification due to MLI [*Fox-Kemper et al.*, 2008; *Mahadevan et al.*, 2010] is an order of magnitude larger than that accompanying the geostrophic

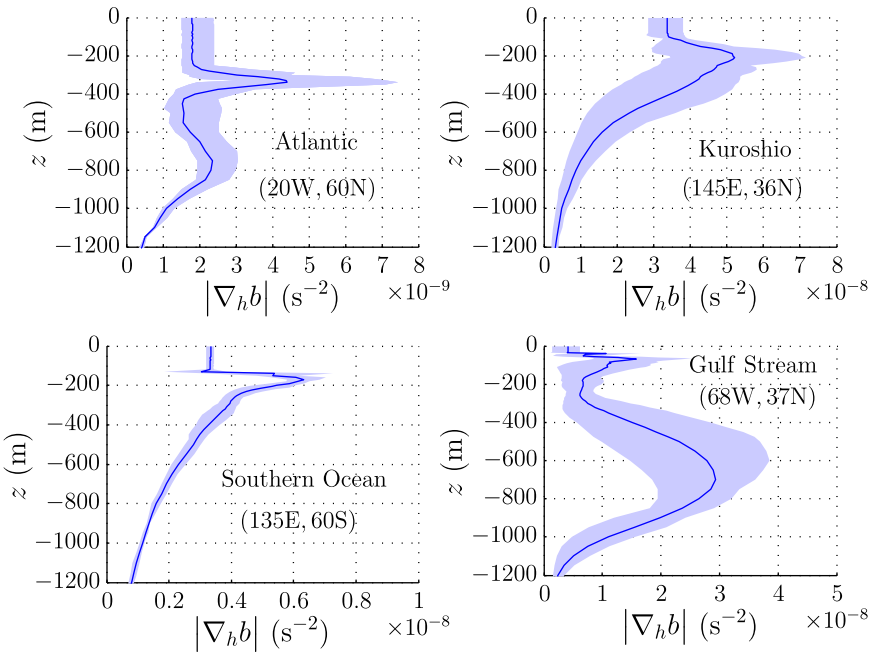

Figure 1. Vertical profiles of lateral buoyancy gradient ($|\nabla_h b|$) during winter months (March/September for the Northern/Southern Hemisphere, respectively) in different oceanic basins from the MIMOC climatology [*Schmidtko et al.*, 2013] of potential density, gridded at 0.5°×0.5°. The solid line shows the mean profile obtained from a 3 × 3 stencil of profiles spanning a 1°×1° box and centered at the indicated location. The shaded region shows the spread about this mean value. The chosen locations in the Atlantic and the Gulf Stream correspond to the sites in the North Atlantic Bloom experiment [*Mahadevan et al.*, 2012] and the LATMIX-2012 experiment [*Özgökmen et al.*, 2012; *Scherbina et al.*, 2013] while the location in the Kuroshio was the site of an earlier study [*Nagai et al.*, 2012].

slumping of isopycnals [*Tandon and Garrett*, 1994, 1995]. The resultant shoaling of the mixed layer can increase the residence time of the phytoplankton within the euphotic zone, thus initiating phytoplankton blooms in wintertime conditions where deep mixed layers typically limit the access of the upper ocean to light [*Mahadevan et al.*, 2012; *Taylor and Ferrari*, 2011]. The slumping of isopycnals from MLI can be countered by downfront winds through the Ekman transport of heavier over lighter fluid [*Thomas*, 2005; *Mahadevan et al.*, 2010]. Under such conditions, MLI continue to restratify the upper ocean but the possibility now exists of a dynamic equilibrium between the wind and eddies [*Mahadevan et al.*, 2010].

Though several numerical studies have analyzed MLI (see section 1) for fronts confined to the mixed layer, lateral buoyancy gradients need not vanish below the mixed layer. In Figure 1, we plot the magnitude of the lateral buoyancy gradient, $|\nabla_h b|$, inferred from the MIMOC [*Schmidtko et al.*, 2013] Argo-based climatology, which has a spatial resolution of 0.5°×0.5°. We choose wintertime conditions with O(100 m) mixed layers as they are representative of the numerical studies cited in section 1. A few comments regarding the climatologies from Argo floats are in order. They describe lateral gradients over scales spanning 50 km or larger. Thus, at most latitudes, they severely understate submesoscale variability and to a lesser extent, mesoscale variability. Additionally, some of the inferred lateral variation could reflect nonfrontal features, such as lateral variations in the mixed-layer depth or the peak stratification in the pycnocline. For instance, a combination of these factors is likely at play behind the sharp increase in the magnitude of lateral gradients immediately below the mixed-layer base (Figure 1). There are other features, however, that mirror those recorded by in situ observations. Measurements in the Kuroshio [*Nagai et al.*, 2012] show significant baroclinic gradients below the mixed layer. In the Gulf Stream, the secondary peak in $|\nabla_h b|$ below the mixed layer (Figure 1) has also been observed in measurements (figure not shown) from the LineW program (operated by the Woods Hole Oceanographic Institution). Hence, the Argo-based climatologies, while not direct evidence, are suggestive of the presence of baroclinicity below the mixed layer, as confirmed by in situ measurements.

The APE within the mixed layer and in the interior fuel different instabilities with their characteristic temporal and spatial scales. In the mixed layer, the APE is the source of MLI, discussed earlier. For midlatitudes,

assuming an O(1) balanced Richardson number, linear theory [*Stone*, 1970] predicts length and time scales of O(1–10 km) and O(1 day), respectively, for the eddies resulting from MLI. The numerical studies cited earlier validate these estimates. The APE in the interior drives quasi-geostrophic baroclinic instability (QGBI) [*Charney*, 1948], creating O(10–100 km) mesoscale eddies with growth time scales on the order of weeks to months [*Smith*, 2007; *Tulloch et al*., 2011]. This raises the possibility that at deep fronts (fronts persisting to depths below the mixed layer), the fast, ageostrophic dynamics within the mixed layer could potentially couple with the slower, QG dynamics below it over sufficiently long time scales. Such coupling can have important consequences. The vertical buoyancy fluxes due to MLI alone are maximum within the central region of the mixed layer [*Fox-Kemper et al*., 2008; *Mahadevan et al*., 2012] and negligible at its base. Coupling between the mixed layer and the interior, however, could give rise to enhanced vertical buoyancy fluxes near the base of the mixed layer. Similar arguments suggest deep fronts could enhance the transport of tracers into the upper ocean through tracer fluxes at the base of the mixed layer. The potential for mesoscale-submesoscale (hereafter meso-submeso) coupling has implications for general circulation models (GCMs) where the grids are too coarse to resolve even the mesoscale spectrum completely. Such GCMs typically employ separate parameterizations for the submesoscale circulation in the mixed layer [*Fox-Kemper et al*., 2008] and the mesoscale circulation in the interior [*Gent and McWilliams*, 1990]. The parameterization by *Fox-Kemper et al*. [2008] reproduces, in an average sense, the slumping of isopyncals due to MLI while the Gent-McWilliams scheme represents the slumping of isopycnals in the interior due to QGBI. The presence of meso-submeso coupling, therefore, raises the issue whether existing parameterizations for submesoscale and mesoscale eddies can capture such dynamics.

In this study, we undertake idealized numerical experiments to explore meso-submeso coupling at deep fronts. Our experiments simulate fronts in a weakly stratified mixed layer forced by downfront winds and overlying a strongly stratified interior. To simulate deep fronts, we extend the baroclinicity into the stratified interior where the lateral buoyancy gradient attenuates with depth. The deep-front simulations differ in their peak stratification just below the mixed-layer base. The study addresses two issues: (i) the potential for meso-submeso coupling at deep fronts; and (ii) the implication of such coupling for the exchange of buoyancy and tracer between the mixed layer and the interior. We contrast the evolution of the buoyancy fluxes with and without meso-submeso coupling, highlighting the important differences. This is followed by a discussion of how such coupling bears on existing parameterizations of submesoscales and mesoscales in noneddy-resolving models. We conclude with a discussion of the implications of meso-submeso coupling for the evolution of tracer fluxes.

2. Modeling

For notational ease, we switch between the indexed and the conventional representation of variables when necessary. For instance, the symbols $\{x_i, (i=1,2,3)\}$ and (x, y, z) are equivalent as are $\{u_i, (i=1,2,3)\}$ and (u, v, w).

2.1. Model Equations

The Process Study Ocean Model, or PSOM, is a three-dimensional (3-D), nonhydrostatic model [*Mahadevan*, 2006] where the top layer of grid cells follows the free surface. For the discretization, the code uses Quadratic Upstream Interpolation for Convective Kinematics (QUICK) [*Leonard*, 1988], a scheme known for its small numerical diffusion and dispersion. A description of the model variables follows. Variables with the tilde operator represent resolved-scale variables and those without the tilde operator represent subgrid-scale (SGS) fields. The model equations in nondimensional form are:

$$D_t\tilde{\rho} = \tilde{F}\tilde{\rho} - \frac{\partial \tau_i^{\rho}}{\partial x_i} \tag{1}$$

$$D_t\tilde{u} + Ro^{-1}(\tilde{p}_x + \gamma\tilde{q}_x^* - f\tilde{v} + Ro\,\delta\, b\tilde{w}) = \tilde{F}^x - \frac{\partial \tau_{ij}^d}{\partial x_j}\ ;\ i=1 \tag{2}$$

$$D_t\tilde{v} + Ro^{-1}(\tilde{p}_y + \gamma\tilde{q}_y^* + f\tilde{u}) = \tilde{F}^y - \frac{\partial \tau_{ij}^d}{\partial x_j}\ ;\ i=2 \tag{3}$$

$$D_t\tilde{w}+Ro^{-2}\delta^{-1}\left(\frac{\gamma}{\delta}\tilde{q}^*_z-b\tilde{u}\right)=\tilde{F}^z-\frac{\partial\tau^d_{ij}}{\partial x_j}\ ;\ i=3 \tag{4}$$

$$\tilde{u}_x+\tilde{v}_y+Ro\,\tilde{w}_z=0 \tag{5}$$

where $D_t \equiv \partial_t+\tilde{u}\partial_x+\tilde{v}\partial_y+Ro\,\tilde{w}\partial_z$ is the nondimensional material derivative operator. The variables $\tilde{u}, \tilde{v}$, and $\tilde{w}$ denote the nondimensional filtered velocity components along the eastward (x), northward (y), and upward (z) directions, respectively, on the earth's surface. The variable $\tilde{\rho}$ denotes the filtered density perturbation from the background stratification prescribed at $t=0$. The components of the Coriolis acceleration scaled with the earth's angular velocity, Ω, are denoted by $f=2\sin(\phi)$ and $b=2\cos(\phi)$, where ϕ is the latitude. Defining U, W, L and D to be the relevant scales for the horizontal velocity, vertical velocity, the horizontal and vertical length scales, respectively, the nondimensional parameters in the model are: (i) the Rossby number, $Ro=U/\Omega L$, where Ω is the angular velocity of rotation of the earth; (ii) ratio of the nonhydrostatic (NH) to hydrostatic (HY) pressure variations, $\gamma=Q/P$, where Q and P are the characteristic scales for the NH and HY components, respectively; and (iii) the aspect ratio, $\delta=D/L$. For the NH runs, it is appropriate to set $\gamma=\delta$ [*Mahadevan*, 2006]. The filtered HY component is denoted by $\tilde{p}$ and the filtered, modified NH component (discussed below) by $\tilde{q}^*$. Setting $\gamma=0$ turns off the NH effects. By definition, $\tilde{p}$ satisfies $\tilde{p}_z+\tilde{\rho}g=0$, where g is the acceleration due to gravity. Scaling the vertical vorticity equation and assuming a balance between the advection and divergence terms yields $W=Ro\delta U$ [*Mahadevan*, 1996].

The forcing terms are shown on the right-hand side of (1)–(4) as $\tilde{F}^\rho, \tilde{F}^x$ and so on. In this study, there is no heating or cooling at the surface, and we include the wind stress in the momentum equation as a boundary condition on the subgrid momentum stress (described below) at the upper boundary. Hence, the forcing terms $\tilde{F}^\rho, \tilde{F}^x$, etc. are zero. The nondimensional SGS density fluxes are denoted by $\tau^\rho_i=\widetilde{\rho u_i}-\tilde{\rho}\tilde{u}_i$. We denote the deviatoric nondimensional SGS momentum stress tensor as $\tau^d_{ij}=\widetilde{u_iu_j}-\tilde{u}_i\tilde{u}_j-(2/3)\delta_{ij}e_{sgs}$, where δ_{ij} is the Kronecker-Delta operator and $e_{sgs}=\widetilde{u_iu_i}-\tilde{u}_i\tilde{u}_i$ is the nondimensional SGS kinetic energy. By construction, τ^d_{ij} is traceless. The variable $\tilde{q}^*$ is the modified, filtered NH component of pressure as it includes a contribution from $(2/3)e_{sgs}$, in addition to the true NH pressure component. To close (1–4), we parameterize the three SGS fluxes and the six independent SGS stresses using an anisotropic version of the Smagorinsky model [*Roman et al.*, 2010; *Ramachandran et al.*, 2013]. Our choice of the SGS model, unlike other SGS closures (e.g., $k-\epsilon$ closures), does not require knowledge of e_{SGS} to compute the subgrid viscosities. Hence, we do not parameterize e_{SGS} in this study.

2.2. Model Configuration

Our simulations (Table 1) evolve the model equations (section 2.1) for a density front initially in thermal-wind balance with a westerly jet (Figure 2). The front is forced by downfront winds which, through Ekman advection of heavier over lighter fluid, attempt to counter the restratification by MLI. For the simulation without deep fronts, the westerly jet decreases to zero at the base of a weakly stratified mixed layer. The surface winds have a fixed magnitude and direction but their alignment with the front changes continuously as the front meanders. The magnitude of the winds is maximum at the front, midway between the northern and the southern boundaries, and tapers to zero (sinusoidally) in either direction toward those boundaries. The winds decrease to zero a few grid cells ahead of the meridional boundaries to ensure the wind stress curl is exactly zero within some buffer region near the wall. We impose such a meridional variation on the magnitude of the winds to minimize the Ekman upwelling and downwelling near the northern and southern boundaries.

For fronts confined to the mixed layer, we prescribe a south-to-north (S-N) density gradient, constant within the mixed layer and zero beneath (Figure 2). At any depth within the mixed layer, the frontal gradient is maximum at the center of the domain and decays toward the meridional boundaries. For the simulations with deep fronts, we allow the frontal gradient to extend below the mixed layer before tapering it gradually to zero (Figure 3). The maximum lateral buoyancy gradient is the same for simulations with and without deep fronts. The APE residing in the front varies with time, thereby allowing the submesoscale dynamics to feed back onto the mesoscale flow structures. We vary the peak stratification, N^2_{max}, across the deep-front simulations by an order of magnitude to explore its influence on meso-submeso coupling (Table 2).

We introduce two tracers such that at $t=0$ one of them (tracer-1) varies linearly from 1 (bottom) to 0 (top) while the other (tracer-2) varies linearly from 1 (South) to 0 (North). We focus mostly on tracer-1 on account of its relevance to biogeochemical nutrients in the ocean. The choice of a linear profile for tracer-1, instead of more

Table 1. Parameters Held Constant for All Simulations

Simulation parameters		
Description	Symbol	Value
Time step	Δt	216 s
Domain size (zonal)	L_x	96 km
Domain size (meridional)	L_y	192 km
Domain size (vertical)	L_z	500 m
Grid spacing (zonal, meridional)	$\Delta x, \Delta y$	500 m
Grid spacing (vertical)	Δz	3.6 m (near surface) 35 m (bottom)
Mixed-layer depth	z_{MLD}	100 m (initial value)
Westerly wind stress	τ_x	0.1 N m^{-2} (amplitude)
Coriolis parameter	f_0	10^{-4} s^{-1}
Peak lateral buoyancy gradient	$\partial b/\partial y$	0.9×10^{-7} s^{-2} (Initial value)
Mixed-layer stratification	N^2_{ML}	10^{-6} s^{-2}

realistic profiles with depth-varying gradients, simplifies the interpretation of the tracer fluxes in terms of the eddy dynamics.

3. Eddy Stream Function at a Mixed-Layer Front

Using overbars to denote zonal averaging and primes to denote fluctuations from the zonal averages, the time evolution of the zonally averaged buoyancy field, $\bar{b}$, is given by:

$$\frac{\partial \bar{b}}{\partial t} + \bar{\mathbf{u}}.\nabla \bar{b} = -\nabla.(\overline{\mathbf{u}'b'}) \tag{6}$$

From residual mean theory [*Plumb and Ferrari*, 2005], the eddy flux $\overline{\mathbf{u}'b'}$ can be split into a skew flux $\mathrm{F}_{\mathrm{skew}} \equiv \psi_e \hat{\mathbf{i}} \times \nabla b$ [*Griffies*, 1998], where ψ_e is an eddy stream function, and a residual flux equal to the difference between the total and the skew flux. By construction, the skew flux is oriented along isopycnals and describes adiabatic stirring by a divergence-free "bolus" velocity [*Gent and McWilliams*, 1990; *Middleton and Loder*, 1989]. The partitioning between the skew and residual components reflects the extent to which the mechanism generating the fluxes is adiabatic.

Earlier numerical studies [*Fox-Kemper and Ferrari*, 2008; *Mahadevan et al.*, 2010] have shown the eddy buoyancy fluxes generated by MLI are largely adiabatic. In the absence of forcing, these fluxes accomplish rapid restratification of the mixed layer on inertial time scales [*Boccaletti et al.*, 2007]. The ageostrophic, frontal slumping can be described by a circulation that transports, on average, lighter over heavier fluid. For a front oriented along the *x* axis (zonal direction), *Fox-Kemper et al.* [2008] parameterize this restratifying circulation through an eddy stream function, $\psi_{\mathrm{BFK}} = 0.06 z^2_{\mathrm{MLD}} \overline{b_y} \mu(z)/f$, where z_{MLD} is the mixed-layer depth and $\bar{b}_y$ is the zonally averaged frontal buoyancy gradient. The function $\mu(z)$ is a fourth-order shape function that is equal to zero at the surface and vanishes below the mixed-layer base. The parameterization by *Fox-Kemper et al.* [2008] is intended for use in coarse-resolution models that do not resolve submesoscale eddies and represents the contribution to ψ_e

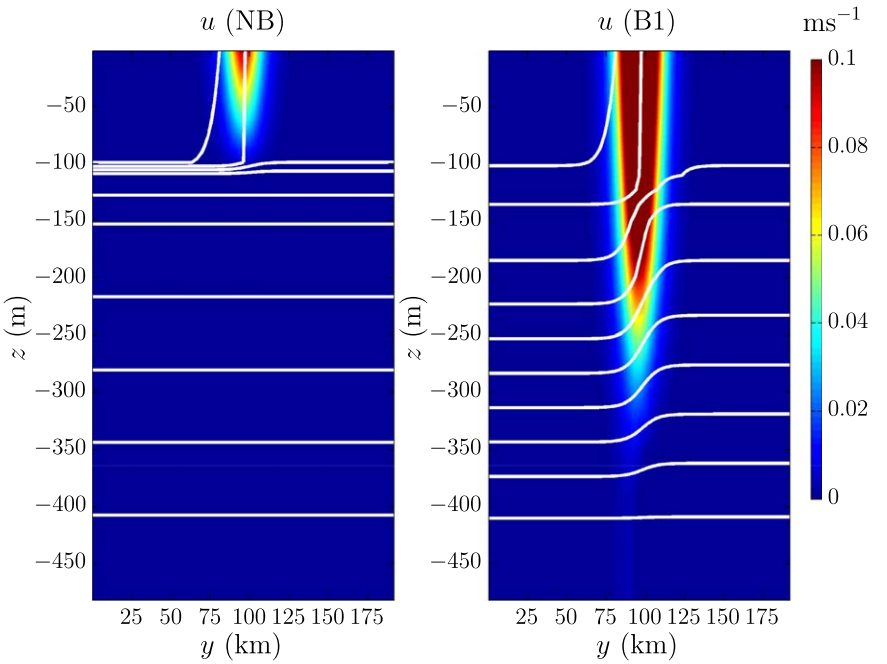

Figure 2. The initial potential density field is in thermal-wind balance with a westerly geostrophic jet. The white lines are contours of $\sigma = \rho - 1000$ (kg m^{-3}) in increments of 0.1 kg m^{-3}. (left) Buoyancy gradients are confined to the mixed layer (simulation NB). (right) Buoyancy gradients persist below the mixed layer (simulation B1).

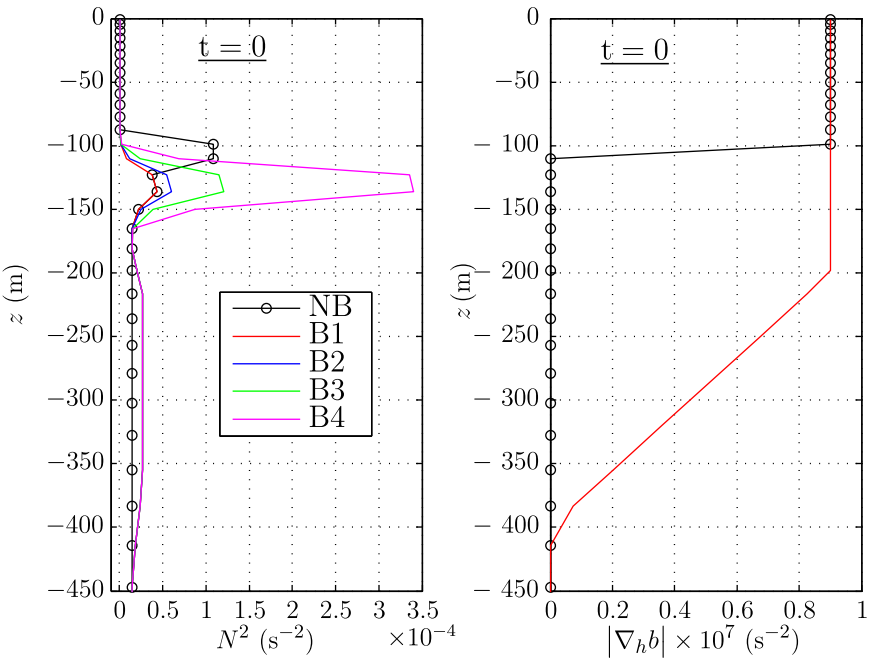

Figure 3. Initial vertical profiles of (left) N^2 and (right) $|\nabla_h b| \times 10^7$ at the initial location of the front, $y = y_f = 96$km, where $|\nabla_h b|$ is the magnitude of the lateral buoyancy gradient. In the left plot, the simulations B1–B4 have identical N^2 below 200 m. In the right plot, simulation NB has no initial lateral density gradients below the mixed layer. The initial vertical profiles of $|\nabla_h b|$ are identical for simulations B1–B4.

from submesoscale restratification. The associated eddy buoyancy fluxes are given by $\psi_{\mathrm{BFK}} \hat{\boldsymbol{i}} \times \nabla b$ [*Gent and McWilliams*, 1990; *Ferrari et al.*, 2008], where $\hat{\boldsymbol{i}}$ is the unit vector along the zonal direction. The ageostrophic slumping due to MLI remains active at fronts forced by downfront winds [*Mahadevan et al.*, 2010]. The ensuing restratification, however, is now in competition with an overturning circulation due to the Ekman transport of heavier over lighter fluid [*Thomas*, 2005]. The stream function $\psi_{\mathrm{wind}} = \tau/(\rho_0 f)$ characterizes the overturning circulation and the associated destratification. The ratio $r = |\psi_{\mathrm{wind}}/\psi_e|$ provides a measure of the dominance of destratification over restratification [*Mahadevan et al.*, 2010]. In submesoscale-resolving simulations, the eddy stream function, ψ_e, can be diagnosed directly as [*Cerovecki et al.*, 2009; *Mahadevan et al.*, 2010]:

$$\psi_e = \alpha \left(\frac{-\alpha \overline{v' b'} \overline{b_z} + \alpha^{-1} \overline{w' b'} \overline{b_y}}{\overline{b_y}^2 + \alpha^2 \overline{b_z}^2} \right), \quad \alpha \ll 1 \tag{7}$$

In (7), the overbars denote averaging in the along-front (here zonal) direction. The expression in (7) extends earlier forms [*Andrews and McIntyre*, 1976; *Held and Schneider*, 1999] to mixed layers, where both lateral and vertical gradients often attain negligibly small values. Simulations with downfront winds confirm the skew flux obtained using ψ_e (from (7)) accounts for the bulk of the total buoyancy flux within the mixed layer, away from the surface [*Mahadevan et al.*, 2010]. Near the surface, the eddy buoyancy fluxes have a large nonskew component due to significant diapycnal exchanges as a consequence of the forcing by winds.

4. Results

The mixed-layer fronts go unstable within a few inertial periods (not shown). The initial frontal meanders from the linear phase of MLI grow in scale due to an inverse cascade [*Fox-Kemper et al.*, 2008] until the meanders scale with the domain. After 31 inertial periods ($tf/(2\pi) = 31$), the spatial structure of the potential density field near the surface and at depth reveals similarities and differences between the simulations without and with deep fronts (Figure 4). Near the surface ($z = -5$m), both sets of simulations show smaller, submesoscale features on the edge of the front coexisting with the domain-scale frontal

Table 2. Parameters Varying Across Simulations

Simulation	Baroclinic Depth (m)	Peak N^2_{max} (s^{-2})
NB	135	1.1×10^{-4}
B1	400	4.4×10^{-5}
B2	400	6.0×10^{-5}
B3	400	1.2×10^{-4}
B4	400	3.4×10^{-4}

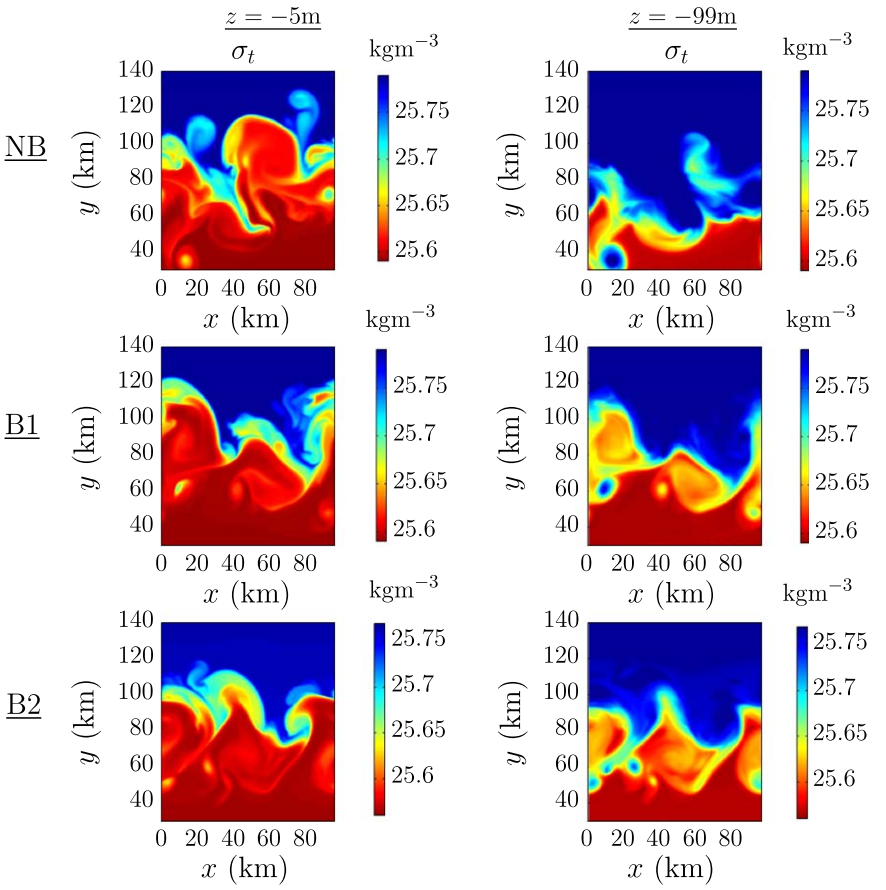

Figure 4. Snapshots of $\sigma_t = \rho - 1000$ for simulations with deep fronts (B1 and B2) and without (NB) at two different depths: (i) $z = -5$m and (ii) $z = -99$m. The snapshots show the fields after 31 inertial periods, $tf/(2\pi) = 31$. The range of values in the plot for B2 are slightly different from those for NB and B1 to better show the lateral gradients. Both simulations with and without deep fronts show submesoscale features superposed on the domain-scale frontal meanders. The similarity between the fields near the surface and at depth is greater for B1 and B2 than for NB, implying greater vertical coherence for B1 and B2.

meanders. The spatial structure of potential density near the surface bears lesser similarity to that deeper down ($z = -99$m) for simulation NB than for the other two simulations. For B1 and B2, the potential density at depth exhibits features similar to those seen near the surface but with diminished amplitude. This shows a greater degree of vertical coherence in the simulations B1 and B2.

Our simulations, either with or without deep fronts, show a rapid enhancement in the vertical and meridional buoyancy flux within the first few inertial periods, consistent with the onset of MLI (Figures 5 and 6).

The differences between the two sets of simulations become apparent at later times due to additional APE in the interior at deep fronts. In both NB and B1, for instance, early on the vertical buoyancy flux has a structure similar to that seen in earlier studies wherein the flux attains its maximum value in the central region of the mixed layer and decreases to zero toward the mixed-layer base [*Fox-Kemper et al*., 2008]. In B1 but not NB, by 30 inertial periods, both lateral and vertical buoyancy fluxes below the mixed layer have become appreciable as QGBI converts the interior APE to eddy kinetic energy. Most importantly, the nonzero buoyancy fluxes near the base of the mixed layer allow the interior to communicate with the upper ocean. We now show the buoyancy fluxes are oriented largely along isopycnals, thus confirming the adiabatic nature of the mechanism (here, QGBI) producing the fluxes.

Having contrasted the simulations with and without deep fronts, we now discuss the differences between the results from the deep-front simulations. At earlier times, both NB and B1 yield a qualitatively similar quadratic-like vertical structure for ψ_e (Figure 7), resembling that for the vertical buoyancy flux (Figure 6). Subsequently, ψ_e departs from near-zero values at the base of the mixed layer. Similar trends are obtained for B2. Unlike B1 and B2, however, B3 and B4 do not yield appreciable ψ_e below the mixed layer. Indeed, for

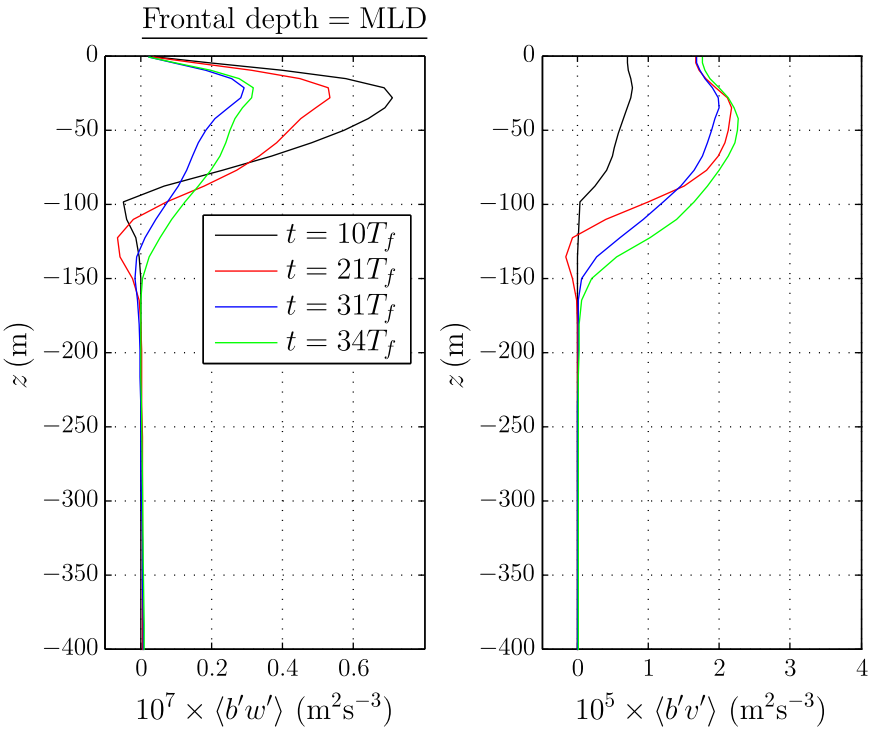

Figure 5. Evolution of the vertical and meridional buoyancy flux for the simulation with frontal gradients confined to the mixed layer. The parameter $T_f = 2\pi/f$ is equal to one inertial period. The progressive increase in the meridional flux and the accompanying decrease in the vertical flux is consistent with a slumping front. Here the slumping is achieved ageostrophically by MLI.

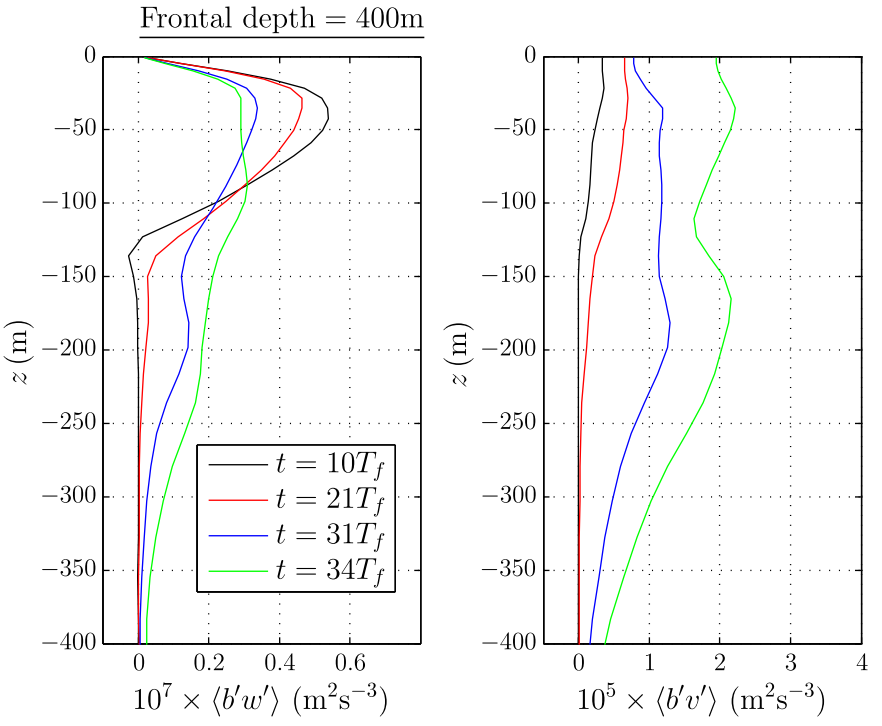

Figure 6. Evolution of the vertical and meridional buoyancy flux for one of the simulations (B1) with deep fronts. The parameter $T_f = 2\pi/f$ is equal to one inertial period. The profiles develop a vertical structure that is fundamentally different from that for NB (Figure 5). The significant departure from near-zero values near the mixed-layer base contrasts NB and earlier studies where the frontal gradients vanished below the mixed layer. It reflects the dynamical coupling between the mixed layer and the interior.

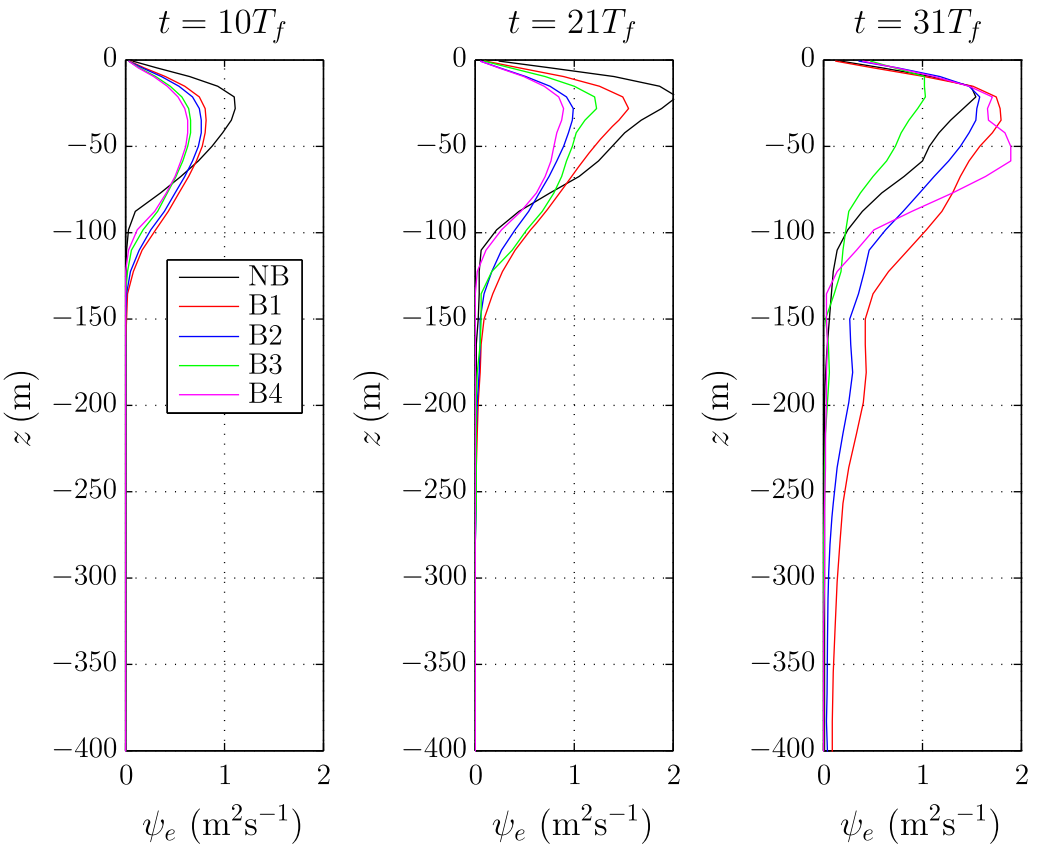

Figure 7. Evolution of the eddy stream function for simulations with and without deep fronts. The parameter $T_f = 2\pi/f$ is equal to one inertial period. The trends are similar to those for the buoyancy fluxes (Figure 6). For the deep-front simulations, the eddy stream function departs from near-zero values at the mixed-layer base, in contrast to NB.

sufficiently strong peak stratification (B4), the vertical structure of ψ_e is indistinguishable from that observed in the simulations without deep fronts (NB). This shows the coupling between the interior and the upper ocean (section 3) is sensitive to the peak stratification, N^2_{max}. In particular, conditions favoring weaker peak stratification are more conducive to meso-submeso coupling. Evaluating the generalized expression for the Eady growth rate [*Tulloch et al.*, 2011] numerically, using lateral gradients in the interior (135–400 m) smoothed to 100 km, yields time scales varying from 15 to 16 inertial periods for all four simulations with deep fronts. This is inconsistent with the dependence of the growth rates on N^2_{max} evident in the simulated results. The differences between the observed growth rates and that predicted by the generalized Eady growth rate could arise potentially due to two factors: (i) forcing by winds; and (ii) interior gradients of potential vorticity. Both these are present in our simulations but are beyond the scope of the canonical Eady problem. We are unable at this stage to quantitatively relate the peak stratification to the time scale for meso-submeso coupling beyond observing lower the stratification, greater the potential for such coupling.

4.1. Orientation of Eddy Buoyancy Fluxes in the Interior

The initial stages of MLI exhibit an Eady phase where the buoyancy fluxes are oriented along a direction corresponding to half the isopycnal slope [*Eady*, 1949; *Fox-Kemper et al.*, 2008]. At later times, the fluxes within the ML tend to align with the isopycnals, which enables their parameterization as a skew flux (section 3). These observations hold for simulations with or without deep fronts. With deep fronts, as noted above, the APE in the interior generates eddies by QGBI. The buoyancy flux vectors for B1 after 31 inertial periods reveal the fluxes are very nearly skew (Figure 8). The residual fluxes are relatively small except in regions where the isopycnal slope changes sign. Therefore, the coupling between the upper ocean and the interior in the deep-front simulations is principally adiabatic.

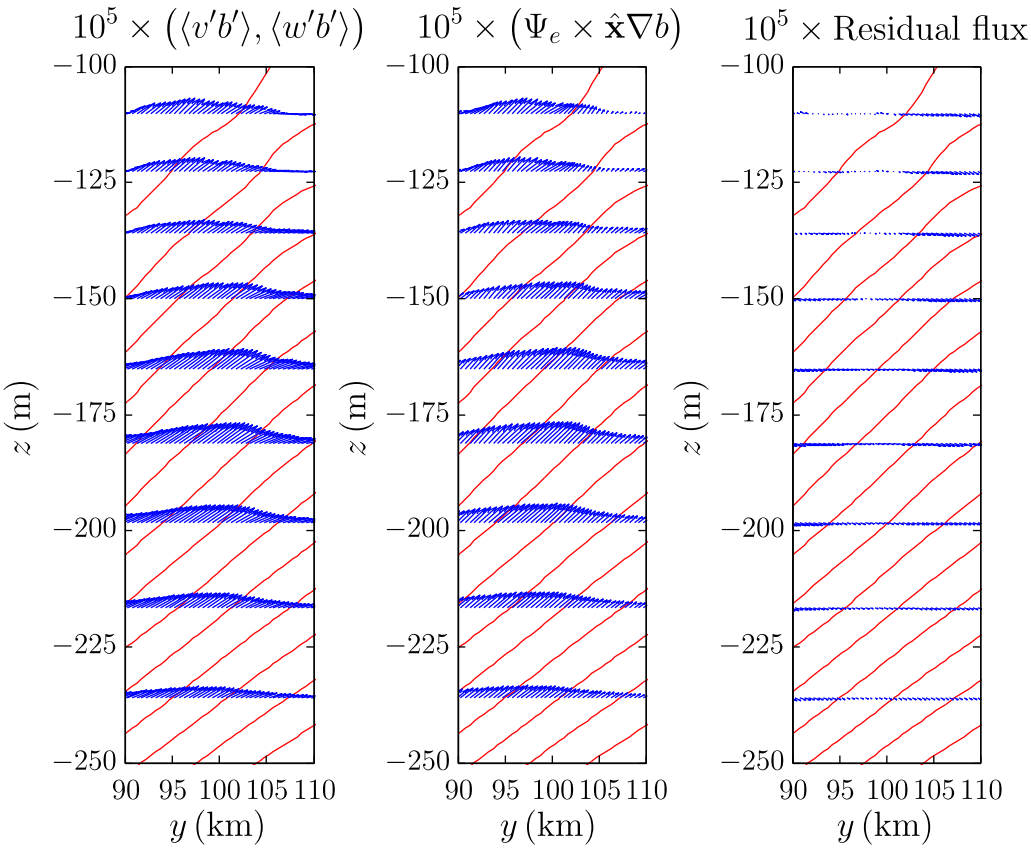

Figure 8. (left) Buoyancy eddy flux vectors overlain on isopycnals after 31 inertial periods. (middle) Skew component of the eddy buoyancy flux. (right) Residual not captured by the skew flux. The eddy buoyancy fluxes result from quasi-geostrophic baroclinic instability and are largely skew with negligible diapycnal exchanges.

4.2. Meso-Submeso Coupling: Implications for the Parameterization of ψ_e

Earlier (section 3), we identified an important difference in the vertical structure of ψ_e between our simulations with significant meso-submeso coupling (B1 and B2) and previous studies [*Fox-Kemper et al.*, 2008; *Mahadevan et al.*, 2010] where the front was confined to the mixed layer. In B1 and B2, ψ_e departs from zero near the mixed-layer base, a property not shared by the eddy stream function in the other simulations or in earlier studies [*Fox-Kemper et al.*, 2008; *Mahadevan et al.*, 2010]. In this section, we briefly discuss whether existing parameterizations for ψ_e reproduce the vertical structure seen here. Presently, noneddy-resolving climate models [*Fox-Kemper et al.*, 2011] represent mesoscale and submesoscale stirring separately through ψ_{GM} [*Gent and McWilliams*, 1990] and ψ_{BFK} [*Fox-Kemper et al.*, 2008], respectively. The Gent-McWilliams stream function [*Gent and McWilliams*, 1990; *Griffies*, 1998], ψ_{GM}, parameterizes adiabatic stirring by mesoscale eddies generated through QGBI in the interior. The stream function ψ_{BFK} parameterizes adiabatic stirring by submesoscale eddies in the mixed layer as a consequence of MLI [*Fox-Kemper et al.*, 2008]. Below the mixed-layer base, ψ_{BFK} is set to zero in its current implementations. A natural question follows: do we obtain the vertical structure of ψ_e at deep fronts from a linear combination of these two parameterizations?

In our simulations, with or without deep fronts, ψ_{BFK} underestimates ψ_e in the mixed layer by factors of 5–10 beyond the first 15–20 inertial periods (plot not shown). One probable reason for this underestimation could be the dominance of Ekman effects over the restratification due to MLI (see section 3). Estimating r using the fields at $t = 0$ yields $r = 1.5$ for all our simulations, which thus belong to a parameter regime where the overturning due to Ekman transport is stronger than that required for equilibrium ($r = 1$). For qualitative comparison, therefore, we plot ψ_e (Figure 9) alongside the sum of $\psi_{\mathrm{param}} = \psi_{\mathrm{wind}}\mu(z) + \psi_{\mathrm{GM}}$, where $\mu(z)$ is a vertical shape function [*Fox-Kemper et al.*, 2008]. The function $\mu(z)$ vanishes at the surface and everywhere below the base of the mixed layer. We interpret $\psi_{\mathrm{wind}}\mu(z)$ as a "scaled up" estimate of ψ_{BFK} corresponding to a simulation where $r = 1$. We compute ψ_{GM} as follows:

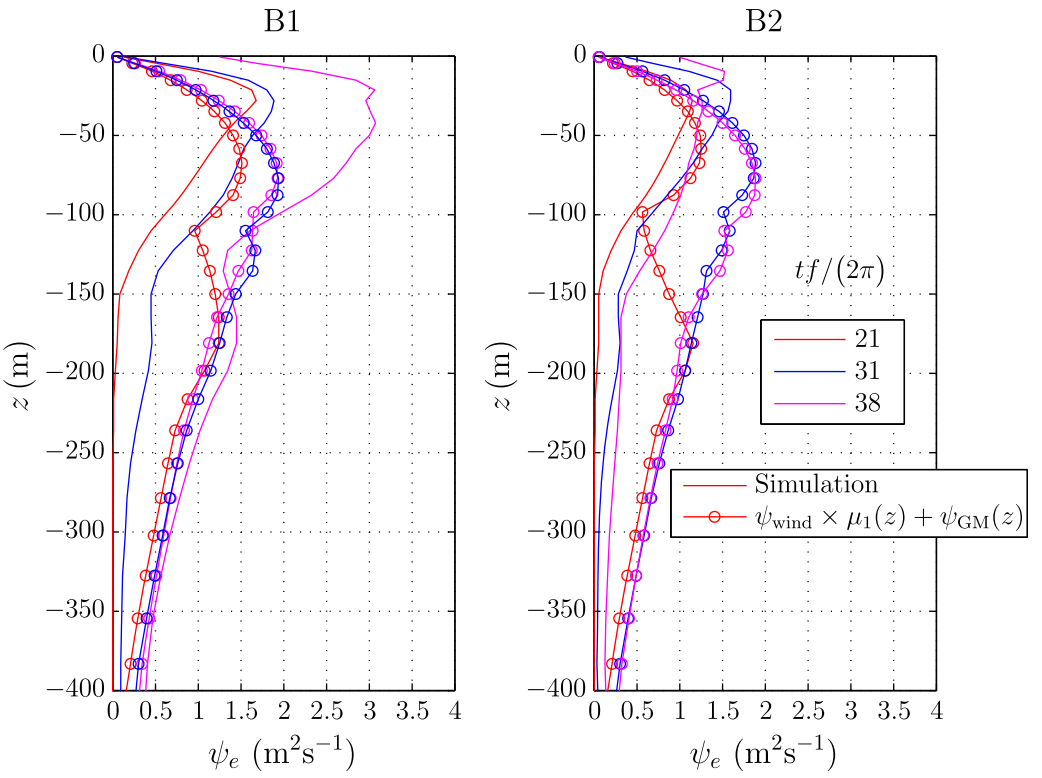

Figure 9. Comparison of the diagnosed eddy stream function (solid lines) for simulations B1 and B2 with $\mu(z)\psi_{\mathrm{wind}}+\psi_{\mathrm{GM}}$ (lines with circles), where $\psi_{\mathrm{wind}}=\tau/(\rho_0 f)$ is the Ekman-induced stream function and $\psi_{\mathrm{GM}}=-k_{\mathrm{GM}}G(z)\partial\bar{b}/\partial y$ is the Gent-McWilliams parameterization [*Gent and McWilliams*, 1990; *Griffies*, 1998] and $G(z)$ is a shape function (equations (25) and (26)) [*Ferrari et al.*, 2008] that tapers ψ_{GM} within the mixed layer to zero at the surface. The function $\mu(z)$ is a vertical shape function [*Fox-Kemper et al.*, 2008] equal to zero at the surface and the mixed-layer base. Beneath the mixed layer, $\mu(z)$ is identically zero. We assume a typical value of $k_{\mathrm{GM}}=10^3\mathrm{m}^2\mathrm{s}^{-1}$ [*Ferrari et al.*, 2008]. The parameterization fails to capture accurately the magnitude and the location of the near-surface maximum in ψ_e. It is also unable, by design, to yield nonzero values at the surface, as observed for ψ_e at later times in the simulation.

$$\psi_{\mathrm{GM}}=k_{\mathrm{GM}}\frac{\overline{b_y}^{100\mathrm{km}}}{\bar{b}_z} \tag{8}$$

where we use the resolved lateral buoyancy gradient scaled down to 100 km, a reasonable scale for the applicability of equation (8). We pick a typical value for the Gent-McWilliams diffusivity $k_{\mathrm{GM}}=10^3\mathrm{m}^2\mathrm{s}^{-1}$ [*Griffies et al.*, 1998; *Ferrari et al.*, 2008] and the form for ψ_{GM} prescribed by *Ferrari et al.* [2008], wherein it tapers linearly above the mixed layer to vanish at the surface. In contrast, ψ_{BFK}, and consequently $\mu(z)$, is finite within the mixed layer and zero beneath it [*Fox-Kemper et al.*, 2008]. For simulation B1, ψ_{param} agrees well with ψ_e after the onset of QGBI in the interior. The agreement is poorer within the mixed layer. In B2, the onset of QGBI occurs later (section 3) and ψ_e grows more gradually in the interior than in the case of B1. At the end of the simulated time period for B2, ψ_{param} in the interior is larger than ψ_e. Within the mixed layer, the agreement with ψ_e is slightly better than for B1. There remain, nevertheless, important differences between ψ_e and ψ_{param} within the mixed layer for both B1 and B2. Near the surface, ψ_e attains nonzero values by 38 inertial periods whereas ψ_{param}, by construction, remains zero at all times. Second, the maxima in ψ_e occur at shallower depths than in ψ_{param}. The two differences between ψ_e and ψ_{param} listed above need not be a consequence of meso-submeso coupling alone as they could potentially arise also due to interactions between winds and MLI. The inability of ψ_{param} to reproduce these two aspects hints at a potential role for Ekman-layer dynamics at density fronts (when $r>1$) not accounted for, by design, in ψ_{BFK}. Thus, an extension of the parameterization by *Fox-Kemper et al.* [2008] for different wind-forced regimes, while beyond the scope of the current study, might improve the prediction by ψ_{param} within the mixed layer.

4.3. Tracer Evolution

One way to quantify the impact of deep fronts on tracers is to compare, in an average sense, the amount of tracer found within the mixed layer among the different simulations. Such a comparison is motivated by

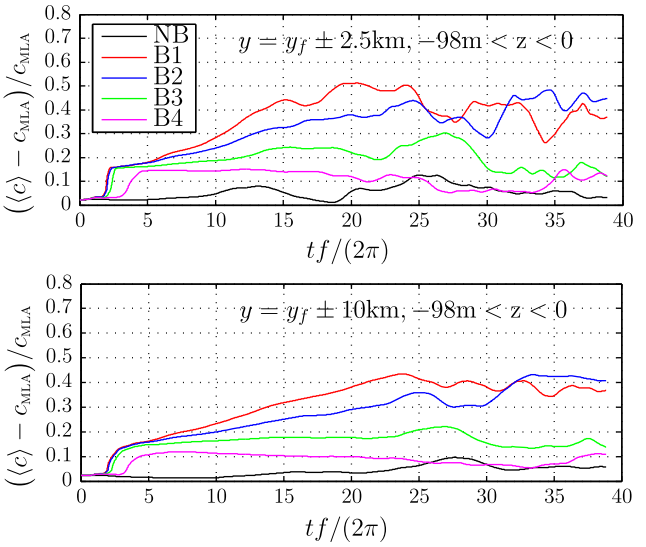

Figure 10. Evolution of the volume-averaged concentration for tracer-1, expressed as the fractional change from c_{MLA}, where c_{MLA} is the average of the initial tracer profile across the mixed layer at $t = 0$. The averaging boxes span 5 and 20 km meridionally (centered at $y = y_f = 96$km), are 98 m deep from the surface, and run the entire zonal extent of the domain. Compared to NB, the deep fronts transport more tracer into the upper layers. Among the deep front simulations, the two with the smallest peak stratification (B1 and B2) yield the largest averaged tracer concentrations in the top 98 m.

the realization tracer-1 could represent nutrient concentrations that are typically high at depth and low near the surface. Within this context, conditions that enhance vertical transport of the tracer from greater to shallower depths assume obvious significance. In the following discussion, we will compute and contrast the volume averages of tracers over different volumes varying in meridional and vertical extent but always spanning the entire zonal extent of the domain. We consider two meridional sizes for the averaging boxes: 5 and 20 km, centered at the initial location of the front ($y = y_f = 96$km). The vertical extent of the boxes is 98 m, which is approximately equal to the initial mixed-layer depth. Together, these choices for the meridional and vertical limits of the averaging volume describe eddying regions of varying sizes within the mixed layer.

Let us denote the initial ($t = 0$) volume average over the mixed layer of tracer-1 as c_{MLA}. The variable c_{MLA} represents the ML tracer concentration that will result as a consequence of a mixing event that homogenizes the tracer vertically within the mixed layer. At later times, the volume-averaged concentration of tracer-1 over an arbitrary volume, $\bar{c}^{xyz}$, can exceed c_{MLA} only through a net influx of tracer into the averaging domain, absent sources or sinks. The influx can be vertical, meridional, or both but not zonal as, by design, the box spans the zonal extent of the zonally periodic domain.

The time evolution of the tracer field does not change significantly with the choice of the meridional averaging length, here 5 and 20 km (Figure 10). Henceforth, we will refer to the results obtained by averaging over 20 km (bottom). The tracer evolution for the different simulations shows significant differences. The volume-averaged tracer for the simulation without deep fronts (NB) barely exceeds c_{MLA} over the entire course of the simulation. This contrasts the simulations B1–B3, all of which yield averaged tracer concentrations larger than c_{MLA}. Among the simulations with deep fronts, the simulations B1 and B2 yield the largest averaged tracer concentrations. Interestingly, the tracer concentrations for the simulations B1–B4 start to exceed those in NB within the first few inertial periods.

Figure 10 shows mixed-layer fronts are less efficient than deep fronts in transporting tracer from depth into the mixed layer. This property of deep fronts to bring more tracer near the surface, on average, also holds true for instantaneous tracer concentrations (Figure 11). The maximum instantaneous values in the top 28 m are typically smaller than those in the top 98 m. This is consistent with more tracer available near 98 m than at 28 m, due to a steep increase in the tracer gradient toward the base of the mixed layer. Within the top 28 m, B1–B4 exhibit larger maximum values than NB. Among B1–B4, the maximum instantaneous values decrease with increasing peak stratification. Within the top 98 m, B1–B3 continue to yield larger maximum tracer concentrations compared to NB. The simulation B4, however, yields smaller values for the same than NB.

4.4. Eddy Tracer Fluxes

A plot of the isopycnally averaged tracer flux vectors in the interior shows fluxes largely along isopycnals (Figure 12). The diffusion of tracers in the interior occurs through a combination of skew (section 4.1) and

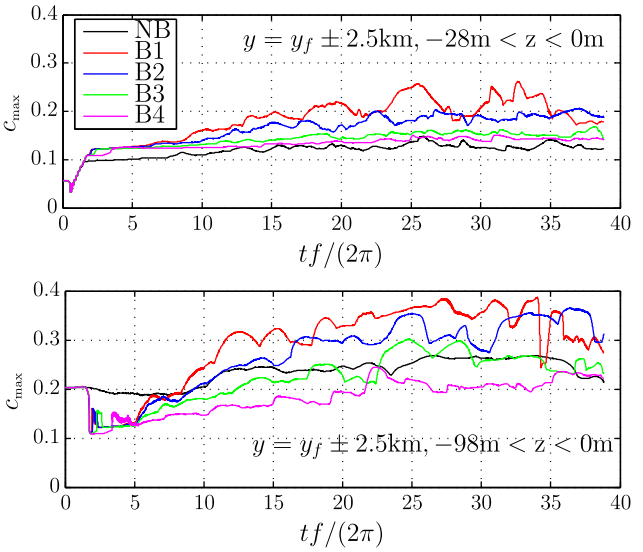

Figure 11. Evolution of the maximum tracer concentration within two volumes. The volumes span 5 km (centered at $y=y_f=96$km), have depths of (top) 28 m or (bottom) 98 m, and run the entire zonal extent of the domain. The trends are similar to that observed for the mean concentrations (Figure 10). Compared to NB, the deep fronts transport more tracer into the upper layers. Among the deep front simulations, the two with the smallest peak stratification (B1 and B2) yield the largest instantaneous tracer concentrations in the top 98 m.

Redi diffusion [*Redi*, 1982], if we neglect exchange of tracer across isopycnals due to diabatic processes. The skew flux for a tracer, $\psi_e \hat{\boldsymbol{i}} \times \nabla c$, where c is the tracer, parameterizes the eddy-induced adiabatic stirring of the tracer along its isolines [*Gent and McWilliams*, 1990], similar to the skew flux for buoyancy discussed earlier (section 3). Skew diffusion is achieved by the off-diagonal components of the eddy-viscosity tensor [*Griffies*, 1998] and does not impact the evolution of any tracer moment other than the mean. Redi diffusion corresponds to the diagonal components of the eddy-viscosity tensor and serves to destroy tracer variance by mixing away tracer gradients along isopycnals. The initial tracer isolines are horizontal but they tend to become aligned with the isopycnals in the interior due to stirring by mesoscale eddies. Given that the eddies in the interior are generated principally by adiabatic processes (Figure 8), we expect the tracer fluxes to be aligned mostly with the isopycnals, as is indeed the case (Figure 12).

Following *Gent and McWilliams* [1990], we use a skew parameterization to estimate the order of magnitude for the tracer fluxes in the interior. Assuming zonally averaged quantities, the skew tracer flux (section 4.1) is equal to $\psi_e \hat{\mathbf{i}} \times \nabla c$, the vector cross product of the eddy stream function, and the tracer gradient. Expanding the cross product yields the following for the individual components:

$$\overline{v'c'} = \psi_e \frac{\partial \bar{c}}{\partial z} \; ; \; \overline{w'c'} = \psi_e \frac{\partial \bar{c}}{\partial y} \tag{9}$$

If we further substitute the Gent-McWilliams form for ψ_e, we obtain:

$$\overline{v'c'} = k_{\text{GM}} \frac{\overline{b_y}}{\overline{b_z}} \frac{\partial \bar{c}}{\partial z} \; ; \; \overline{w'c'} = k_{\text{GM}} \frac{\overline{b_y}}{\overline{b_z}} \frac{\partial \bar{c}}{\partial y} \tag{10}$$

Borrowing our earlier estimation of ψ_{GM} (see section 4.2) and using the initial vertical gradient for tracer-1 yields, $\overline{v'c'} = 3\times10^{-3}$. A nonzero skew vertical flux requires a nonzero meridional tracer gradient. Although the spatial gradients for tracer-1 are primarily in the vertical, even at later times, the tracer field develops nonzero gradients in the meridional direction as the eddies try to align the tracer isolines (initially horizontal) with the isopycnals in the interior. We confirmed this is indeed the case for both the tracers (figure not shown). This observation enables us to infer the meridional tracer gradient as $\overline{c_y} \approx \overline{c_z} \times (\overline{b_y}/\overline{b_z})$ and consequently, the vertical skew flux as $\overline{w'c'} = 5\times10^{-6}$. Repeating this procedure for tracer-2 yields $(\overline{v'c'}, \overline{w'c'}) = (5\times10^{-3}, 8\times10^{-6})$. These calculations provide order of magnitudes for the tracer fluxes that agree well with the simulation results (Figure 13).

5. Conclusions

In this study, we use a set of idealized numerical experiments, motivated by in situ observations and Argo-based climatologies, to explore the potential for meso-submeso coupling at deep fronts, where the frontal gradients persist below the mixed layer. Though previous numerical studies of submesoscale instabilities

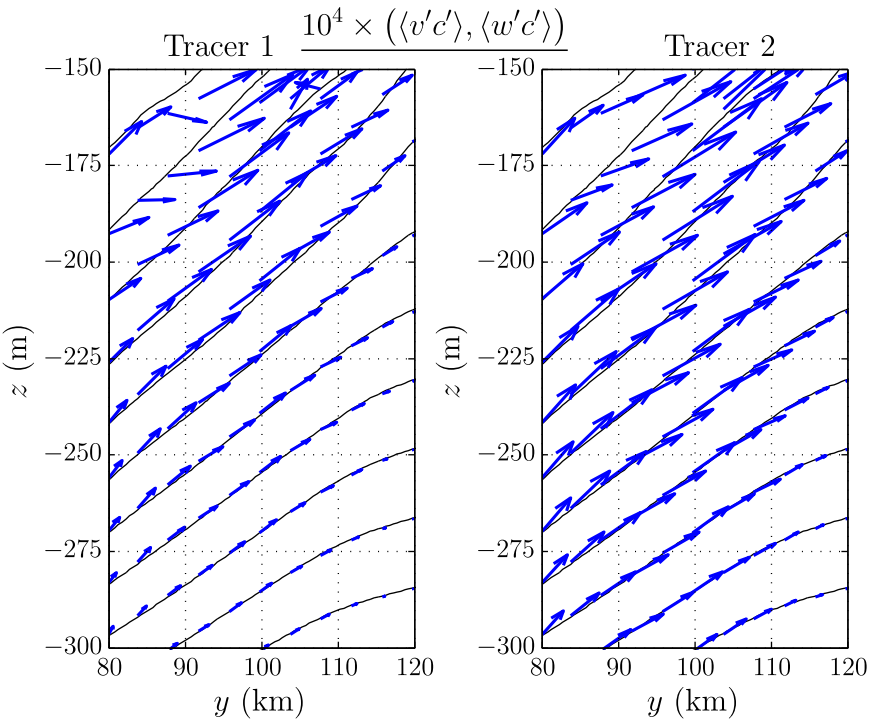

Figure 12. Simulation B1: orientation of tracer fluxes averaged along nonoutcropping isopycnals in the zonal direction after 31 inertial periods. The primed variables are deviations from the corresponding isopycnal average. The isopycnals (black) are spaced 0.04 kg m^{-3} apart. Tracer-1 and Tracer-2 vary linearly in the vertical and meridional directions, respectively, at $t = 0$. The tracer fluxes are nearly aligned with the isopycnals, indicating adiabatic stirring by mesoscale eddies generated from the release of interior APE by quasi-geostrophic baroclinic instability. For magnitudes of the tracer fluxes, see Figure 13.

have focused primarily on fronts confined to the mixed layer, in situ observations, and Argo-based climatologies show frontal gradients frequently persist below the mixed layer. Our simulations show deep fronts can induce meso-submeso coupling through fluxes of buoyancy and tracer along sloping isopycnals. Such fluxes are generated in the interior due to the onset of quasi-geostrophic baroclinic instability, which occurs on slower time scales compared to the submesoscale, frontal instabilities within the mixed layer. On these slower time scales, the mesoscale eddies generated by baroclinic instability in the interior stir material properties along isopycnals, giving rise to buoyancy and tracer fluxes. The buoyancy flux thus generated departs from near-zero values at the mixed-layer base, in contrast to what is observed for fronts confined to the mixed layer. The buoyancy fluxes are mostly skew in both the mixed layer and the interior, with negligible diapycnal components, confirming the adiabatic nature of the release of available potential energy. The time scale over which the meso-submeso coupling occurs increases as the peak stratification increases.

The eddy fluxes of tracer in the interior, like those of buoyancy, are mostly skew and are consistent with order of magnitude estimates from existing parameterizations in the literature. The simulations with and without deep fronts present important differences in the amount of tracer that makes it to the upper mixed layer. The simulations with baroclinicity below the mixed layer yield larger amounts of tracer within the mixed layer, both in an average and instantaneous sense. This enhancement of tracer transport at deep fronts has implications for the exchange of nutrients, dissolved gases (such as O_2 and CO_2) and other biogeochemical tracers between the interior and the surface mixed layer.

Current climate models employ separate parameterizations for the submesoscale circulation in the mixed layer and the mesoscale circulation in the interior, based on the frameworks introduced by *Fox-Kemper et al*. [2008] and *Gent and McWilliams* [1990], respectively. Our results show a linear combination of the parameterizations by *Fox-Kemper et al*. [2008] and *Ferrari et al*. [2008] do not adequately capture the vertical structure of the eddy stream function. In particular, the parameterized stream function is always zero at the surface, in contrast to the diagnosed stream function which departs from zero at later times in the simulation. Additionally, the parameterized stream function attains its maximum at depths greater than those for

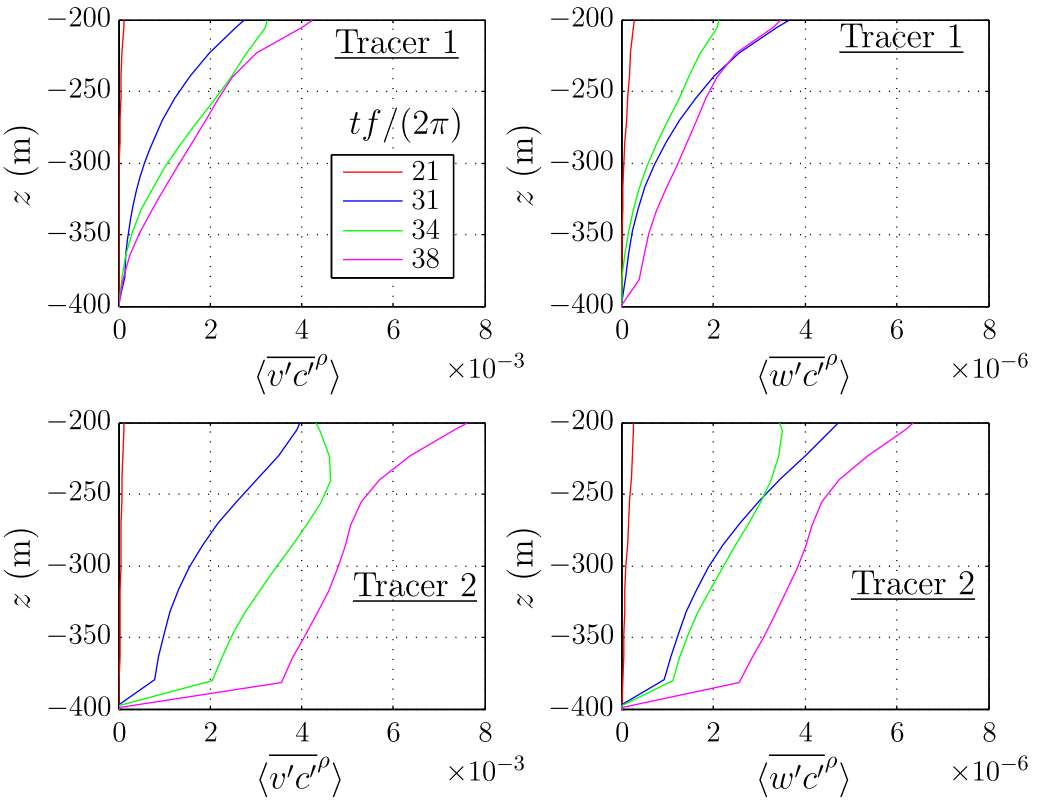

Figure 13. Vertical profiles of isopycnally averaged meridional and vertical tracer fluxes for simulation B1. The averaging is performed in the zonal direction along nonoutcropping isopycnals. Tracer-1 and Tracer-2 vary linearly in the vertical and meridional directions, respectively, at $t = 0$. Due to the skew nature of the fluxes, a nonzero vertical flux implies a nonzero meridional gradient in the tracer field and vice versa. Despite its initial profile, tracer-1 develops a nonzero meridional gradient as the eddies tend to align the tracer contours with the isopycnals. Similar arguments hold for the nonzero meridional flux for tracer-2, which initially has only a meridional gradient but develops a vertical gradient subsequently.

the diagnosed stream function. It is possible these differences could arise, at least partly, due to the effects of Ekman-induced overturning, which is not incorporated in existing submesoscale parameterizations.

Appendix A: Simulation Parameters

In Table 1, we list the physical parameters in our numerical simulations, which follow those in the study by *Mahadevan* [2006].

A1. Choice of Lateral Grid Resolution

The lateral grid resolution resolves the most unstable mode predicted by Stone's analysis of ageostrophic baroclinic instabilities [*Stone*, 1970]. For representative values of $U = 0.1$ m s^{-1}, $f = 10^{-4}$ s^{-1}, and $Ri = 1$, his analysis estimates the wavelength of the most unstable mode as $(2\pi U/f)\sqrt{5(1+Ri)/2}$, or 5.6 km, which is an order of magnitude larger than Δx. The grid resolution is too coarse to resolve length scales associated with symmetric instability [*Taylor and Ferrari*, 2009, 2010] but vertical profiles of the balanced Richardson number, Ri_g, averaged near the front show a rapid increase to values greater than 1 after a few inertial periods, implying the conditions necessary for symmetric instability ($0.25 < Ri_g < 0.95$) are violated soon thereafter. Hence, the role of symmetric instability in our simulations is likely confined to the first few inertial periods.

Appendix B: Boundary Conditions

The boundary conditions are periodic in the zonal direction. The southern and northern boundaries are impermeable walls across which we impose zero advective fluxes and zero meridional gradients of the

velocity, density and, SGS fields. The topmost layer of grid cells follows the free surface [*Mahadevan*, 1996]. The SGS stresses τ^d_{13} and τ^d_{23} at the free-surface satisfy $\tau_x/\rho_0 = \tau^d_{13}$ and $\tau_y/\rho_0 = \tau^d_{23}$, where τ_y is the meridional surface wind stress (zero in this study) and $\rho_0 = 1027$ kg m^{-3} is the reference density. The SGS flux τ^ρ_3 at the surface is set equal to the surface density flux, which in this study is zero due to the absence of cooling or heating at the surface. We model bottom friction using a linear drag, $r_{\text{bot}}(U, V)$, where the constant bottom friction coefficient $r_{\text{bot}} = 5\times10^{-4}$ s^{-1} and (U, V) are the dimensional horizontal velocities.

Appendix C: Forcing and Initial Condition

We impose a downfront, westerly (West to East, or W-E) surface wind that varies sinusoidally in the meridional direction such that it attains its maximum value at the front and decreases to zero toward the southern and northern boundaries. The amplitude of the wind stress, τ_x, ramps up linearly from zero to its maximum value of 0.1 N m^{-2}, over a day.

For fronts confined to the mixed layer, we decrease the frontal gradient rapidly to zero over two vertical grid points immediately below the mixed layer. For simulations with deep fronts, we maintain the mixed-layer lateral density gradient to a depth of 200 m below which it tapers linearly to zero at the level of no motion, chosen here to be 400 m. Below this depth, the isopycnals are flat and there is no vertical shear at $t = 0$.

The stratification N^2 is constant within the ML, reaches a maximum through the pycnocline and decreases to values O(10^{-5} s^{-2}) in the interior. The free-surface elevation is higher on the lighter side to ensure the initial barotropic and baroclinic pressure gradients at the lowest depth of baroclinicity are equal and opposite. To nudge the onset of instabilities, the density front has an initial wiggle in the form of a sinusoidal wave with an amplitude of 100 m and wavelength equal to the zonal extent of the domain.

Acknowledgments

S.R. and A.T. acknowledge financial support from the National Science Foundation (NSF OCE-0928138) and the Office of Naval Research (ONR N00014-09-1-0196, ONR N00014-12-1-0101). A.M. acknowledges funding from the National Science Foundation (NSF OCE-0928617) and the Office of Naval Research (ONR N00014-12-1-0101). We thank Gaurav Khanna at the University of Massachusetts, Dartmouth (NSF, PHY-0902026) for computational support. The MIMOC climatology data are available at http://www.pmel.noaa.gov/mimoc/, and the simulation data are available upon request from the corresponding author. The PSOM code can be downloaded from https://github.com/PSOM.

References

Akitomo, K. (2010), Baroclinic instability and submesoscale eddy formation in weakly stratified oceans under cooling, *J. Geophys. Res.*, *115*, C11027, doi:10.1029/2010JC006125.

Andrews, D., and M. E. McIntyre (1976), Planetary waves in horizontal and vertical shear: The generalized Eliasen-Palm relation and the mean zonal acceleration, *J. Atmos. Sci.*, *33*, 2031–2048.

Boccaletti, G., R. Ferrari, and B. Fox-Kemper (2007), Mixed layer instabilities and restratification, *J. Phys. Oceanogr.*, *37*, 2228–2250.

Capet, X., J. C. McWilliams, M. J. Molemaker, and A. F. Shchepetkin (2008a), Mesoscale to submesoscale transition in the California Current System. Part I: Flow structure, eddy flux and observational tests, *J. Phys. Oceanogr.*, *38*, 29–43.

Capet, X., J. C. McWilliams, M. J. Molemaker, and A. F. Shchepetkin (2008b), Mesoscale to submesoscale transition in the California Current System. Part II: Frontal processes, *J. Phys. Oceanogr.*, *38*, 44–64.

Cerovecki, I., R. A. Plumb, and W. Heres (2009), Eddy transport and mixing on a wind- and buoyancy-driven jet on the sphere, *J. Phys. Oceanogr.*, *39*, 1133–1149.

Charney, J. G. (1948), On the scale of atmospheric motions, *Geophys. Publikasjoner*, *17*, 251–265.

D'Asaro, E., C. Lee, L. Rainville, R. Harcourt, and L. Thomas (2011), Anisotropy and coherent structures in planetary turbulence, *Science*, *332*, 318–322.

Eady, E. T. (1949), Long waves and cyclone waves, *Tellus*, *1*, 33–52.

Ferrari, R., J. C. McWilliams, V. M. Canuto, and M. Dubovikov (2008), Parameterization of eddy fluxes near oceanic boundaries, *J. Clim.*, *21*, 2770–2789.

Fox-Kemper, B., and R. Ferrari (2008), Parameterization of mixed layer eddies. Part II: Prognosis and impact, *J. Phys. Oceanogr.*, *38*, 1166–1179.

Fox-Kemper, B., R. Ferrari, and R. W. Hallberg (2008), Parameterization of mixed layer eddies. Part I: Theory and diagnosis, *J. Phys. Oceanogr.*, *38*, 1145–1165.

Fox-Kemper, B., G. Danabasoglu, R. Ferrari, S. M. Griffies, R. W. Hallberg, M. M. Holland, M. E. Maltrud, S. Peacock, and B. L. Samuels (2011), Parameterization of mixed layer eddies. III: Implementation and impact in global ocean climate simulations, *Ocean Modell.*, *39*, 61–78.

Gent, P. R., and J. C. McWilliams (1990), Isopycnal mixing in ocean circulation models, *J. Phys. Oceanogr.*, *20*, 150–155.

Griffies, S. M. (1998), The Gent-McWilliams skew flux, *J. Phys. Oceanogr.*, *28*, 831–841.

Griffies, S. M., A. Gnanadesikan, R. C. Pacanowski, V. D. Larichev, J. K. Dukowicz, and R. D. Smith (1998), Isoneutral diffusion in a z-coordinate ocean model, *J. Phys. Oceanogr.*, *28*, 805–830.

Held, I. M., and T. Schneider (1999), The surface branch of the zonally averaged mass transport circulation in the troposphere, *J. Atmos. Sci.*, *56*, 1688–1697.

Klein, P., and G. Lapeyre (2009), The oceanic vertical pump induced by mesoscale and submesoscale turbulence, *Annu. Rev. Mar. Sci.*, *1*, 351–375.

Klein, P., B. L. Hua, G. Lapeyre, X. Capet, S. L. Gentil, and H. Sasaki (2008), Upper ocean turbulence from high-resolution 3D simulations, *J. Phys. Oceanogr.*, *38*, 1748–1763.

Leonard, B. P. (1988), Simple high-accuracy resolution program for convective modelling of discontinuities, *Int. J. Numer. Methods Fluids*, *8*, 1291–1318.

Lévy, M., P. Klein, and A. M. Treguier (2001), Impacts of sub-mesoscale physics on production and subduction of phytoplankton in an oligotrophic regime, *J. Mar. Res.*, *59*, 535–565.

Mahadevan, A. (1996), A non-hydrostatic mesoscale ocean model. 1: Well-posedness and scaling, *J. Phys. Oceanogr.*, *26*, 1168–1880.
Mahadevan, A. (2006), Modeling vertical motion at ocean fronts, *Ocean Modell.*, *14*, 222–240.
Mahadevan, A., and D. Archer (2000), Modeling the impact of fronts and mesoscale circulation on the nutrient supply and biogeochemistry of the upper ocean, *J. Geophys. Res.*, *105*, 1209–1225.
Mahadevan, A., and A. Tandon (2006), An analysis of mechanisms for submesoscale vertical motion at ocean fronts, *Ocean Modell.*, *14*, 241–256.
Mahadevan, A., L. Thomas, and A. Tandon (2008), Comment on "eddy/wind interactions stimulate extraordinary mid-ocean plankton blooms," *Science*, *320*, 448.
Mahadevan, A., A. Tandon, and R. Ferrari (2010), Rapid changes in mixed layer stratification driven by submesoscale instabilities and winds, *J. Geophys. Res.*, *115*, C03017, doi:10.1029/2008JC005203.
Mahadevan, A., E. D. Asaro, C. Lee, and M. J. Perry (2012), Eddy-driven stratification initiates North Atlantic spring phytoplankton blooms, *Science*, *337*, 54–58.
Middleton, J. F., and J. W. Loder (1989), Skew fluxes in polarized wave fields, *J. Phys. Oceanogr.*, *19*, 68–76.
Nagai, T., A. Tandon, H. Yamazaki, and M. J. Doubell (2012), Direct observations of microscale turbulence and thermohaline structure in the Kuroshio Front, *J. Geophys. Res. Oceans*, *117*, C08013, doi:10.1029/2011JC007228.
Özgökmen, T. M., A. C. Poje, P. F. Fischer, H. Childs, H. Krishnan, C. Garth, A. C. Haza, and E. Ryan (2012), On multi-scale dispertion under the influence of surface mixed-layer instabilities and deep flows, *Ocean Modell.*, *56*, 16–30.
Plumb, R. A., and R. Ferrari (2005), Transformed Eulerian-mean theory. Part I: Nonquasigeostrophic theory for eddies on a zonal-mean flow, *J. Phys. Oceanogr.*, *35*, 165–174.
Ramachandran, S., A. Tandon, and A. Mahadevan (2013), Effect of subgrid-scale mixing on the evolution of forced submesoscale instabilities, *Ocean Modell.*, *66*, 45–63.
Redi, M. H. (1982), Oceanic isopycnal mixing by coordinate rotation, *J. Phys. Oceanogr.*, *12*, 1154–1158.
Roman, F., G. Stipcich, V. Armenio, R. Inghilesi, and S. Corsini (2010), Large eddy simulation of mixing in coastal areas, *Int. J. Heat Fluid Flow*, *31*, 327–341.
Scherbina, A. Y., E. A. D'Asaro, C. M. Lee, J. M. Klymak, M. J. Molemaker, and J. C. McWilliams (2013), Statistics of vertical vorticity, divergence and strain in a developed submesoscale turbulence field, *Geophys. Res. Lett.*, *40*, 4706–4711, doi:10.1002/grl.50919.
Schmidtko, S., G. C. Johnson, and J. M. Lyman (2013), MIMOC: A global monthly isopycnal upper-ocean climatology with mixed layers, *J. Geophys. Res.*, *118*, 1658–1672, doi:10.1002/jgrc.20122.
Smith, S. (2007), The geography of linear baroclinic instability in earth's oceans, *J. Mar. Res.*, *65*, 655–683.
Stone, P. H. (1970), On non-geostrophic baroclinic stability: Part II, *J. Atmos. Sci.*, *27*, 721–726.
Tandon, A., and C. Garrett (1994), Mixed layer restratification due to a horizontal density gradient, *J. Phys. Oceanogr.*, *24*, 1419–1424.
Tandon, A., and C. Garrett (1995), Geostrophic adjustment and restratification of a mixed layer with horizontal gradients above a stratified layer, *J. Phys. Oceanogr.*, *25*, 2229–2241.
Taylor, J. R., and R. Ferrari (2009), On the equilibriation of a symmetrically unstable front via a secondary shear instability, *J. Fluid Mech.*, *622*, 103–113.
Taylor, J. R., and R. Ferrari (2010), Buoyancy and wind-driven convection at mixed layer density fronts, *J. Phys. Oceanogr.*, *40*, 1222–1242.
Taylor, J. R., and R. Ferrari (2011), Ocean fronts trigger high latitude phytoplankton blooms, *Geophys. Res. Lett.*, *38*, L23601, doi:10.1029/2011GL049312.
Thomas, L. (2005), Destruction of potential vorticity by winds, *J. Phys. Oceanogr.*, *35*, 2457–2466.
Thomas, L. N., and J. R. Taylor (2010), Reduction of the usable wind-work on the general circulation by forced symmetric instability, *Geophys. Res. Lett.*, *37*, L18606, doi:10.1029/2010GL044680.
Tulloch, R., J. Marshall, C. Hill, and K. S. Smith (2011), Scales, growth rates and spectral fluxes of baroclinic instability in the ocean, *J. Phys. Oceanogr.*, *41*, 1057–1076.